Supporting information

1 Experimental section

Dissolve 66.38 g $NiSO_4 \cdot 6H_2O$, 2.13 g $MnSO_4 \cdot H_2O$, 0.84 g $Al_2(SO_4)_3$, 0.35 g $MgSO_4 \cdot H_2O$, 1.37 g $Nb(HC_2O_4)_5$ and 0.85 g $(NH_4)_6Mo_7O_{24} \cdot 4H_2O$ in pure water to a volume of 200 mL as a precursor solution. Then the precursor solution was slowly added into the reactor for co-precipitation reaction, wherein 0.6 $mol \cdot L^{-1}$ ammonia water was used as the base liquid, 8 $mol \cdot L^{-1}$ NaOH was used as the pH regulator, and 3 mol L^{-1} ammonia water was used as the complexing agent. The inversion temperature is controlled at 60 °C, pH = 11, and the reaction is carried out for 24 hours. The precursor is then filtered and dried to obtain the precursor. The precursor is mixed with LiOH and ground, and then thermally annealed in pure O_2.

2 Theoretical calculations

2.1 DFT calculation

All the calculations are performed in the framework of the density functional theory with the projector augmented plane-wave method, as implemented in the Vienna ab initio simulation package[1]. The generalized gradient approximation proposed by Perdew, Burke, and Ernzerhof is selected for the exchange-correlation potential[2]. The long range van der Waals interaction is described by the DFT-D3 approach[3]. The cut-off energy for plane wave is set to 500 eV. The energy criterion is set to 10^{-6} eV in iterative solution of the Kohn-Sham equation. The Brillouin zone integration is performed using a 2×2×1 k-mesh. The coulomb interaction potential were used to describe the All the structures are relaxed until the residual forces on the atoms have declined to less than 0.03 eV/Å. To correct the self-interaction error of TM d-orbitals, a Hubbard U term (DFT +U) was included and the U values of 5.9, 5.1, 5.0, and 5.0 eV were adopted for Ni, Mn, Mo and Nb, respectively. The red ball, gray ball, green ball, purple ball, light blue ball, orange ball, pink ball, and dark green ball represent O, Ni, Li, Mn, Al, Mg, Mo, Nb

2.2 Lattice change rate calculation

As shown in Figure 3(a-c), the XRD diffraction peak corresponding to the a-axis

direction of the crystal (2θ is between 64.5-65.5°) shows very small changes. The XRD diffraction peak corresponding to the c-axis direction of the crystal (2θ is between 17-20°) shows fluctuations. We accurately calculated the maximum harmful change value in the c-axis direction according to the following formulas (Eq. S1 and Eq. S2) (Figure 5(d)).

$$2dsin\theta = n\lambda \quad \text{(Eq. S1)}$$

$$d = \frac{1}{\sqrt{\frac{4}{3}(h^2 + hk + k^2)/a^2 + l^2/c^2}} \quad \text{(Eq. S2)}$$

Among them, n=1, λ=1.5406, (hkl) is the crystal plane index, the c-axis corresponds to (003), and the a-axis corresponds to (110).

2.3 Formation energy calculation

The formation energy is calculated according to the formula:

$$E_{form} = E_{Li_xNCM} - xE_{LNCM} - (1-x)E_{NCM} \quad \text{(Eq. S3)}$$

E_{Li_xNCM}, E_{LNCM} and E_{NCM} represent partial lithiation, complete lithiation and complete detachment, respectively. The calculation results are shown in Figure 6.

3. Electrochemical measurements

LIR2016 cell was assembled to study the electrochemical performance of the material. The cathode material, super P and PVDF are coated on the surface of the aluminum foil at a mass ratio of 8:1:1 as cathode, and the lithium metal sheet is used as the anode; the content of active material in the cathode is about 2 mg·cm^{-2}. The electrolyte is 1.0 M $LiPF_6$ in EC/DEC=1:1 (v/v) and purchased from Suzhou Duoduo Chemical Technology Co., Ltd.; Electrochemical tests were carried out on a galvanostatic charge-discharge system (LAND) with a voltage range of 2.8-4.3V. When the battery is tested at 1C (150 mA·g^{-1}) cycle performance, it is first activated at 0.1C. All electrochemical performance tests were performed at room temperature.

4. Material characterization

The morphology of the samples was examined using scanning electronic microscopy (SEM, TESCAN MIRA LMS) and transmission electronic microscopy

(TEM, FEI Tecnai G2 F20) including element distribution by EDS. The crystal structures of the samples were identified using X-ray diffraction (XRD, Rigaku Miniflex 600) within a 2θ range of 10°−80°. In situ XRD testing was performed at Rigaku MiniFlex 600. The surface structure of the cathodes was identified by X-ray photoelectron spectroscopy (XPS, Thermo Scientific K-Alpha, USA). X-ray absorption near edge structure (XANES) measurements of samples were carried out at Shanghai Synchrotron Facility (SSRF).

The composition and element contents of HE-LNM are shown in Table S1, The molar ratio of Ni:Mn:Al:Mg:Nb:Mo is 0.915:0.0475:0.0106:0.0106:0.0068:0.0095.

Table S1. Content of metal elements in HE-LNM

Elements	Ni	Mn	Al	Mg	Nb	Mo
Content (wt.%)	50.833	2.475	0.285	0.247	0.593	0.874

The size distribution of HE-LNM is shown in Figure S1, and the volume average particle size is 6.46 μm.

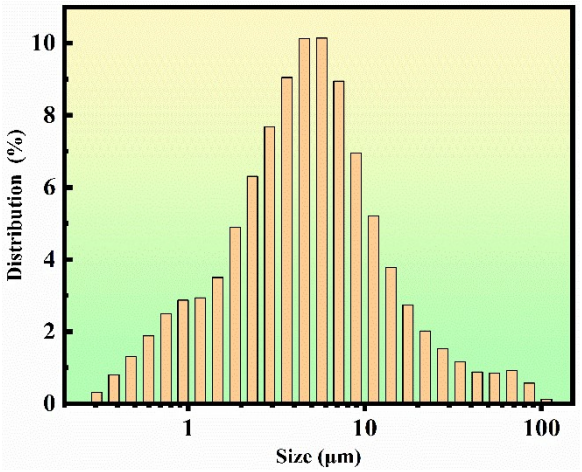

Figure S1 Particle size distribution.

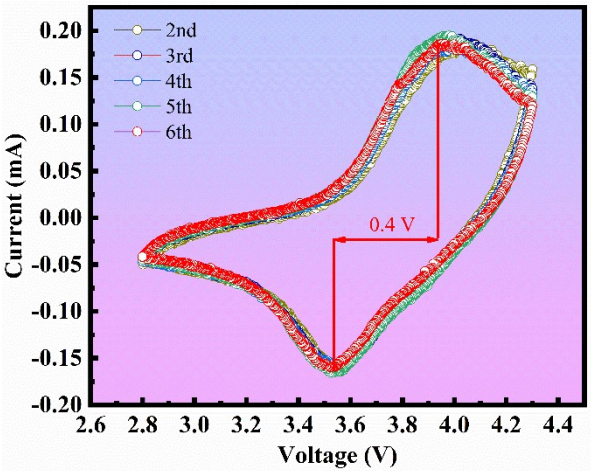

Figure S2 CV curves of HE-LNM.

The CV curve of HE-LNM is shown in Figure S2. Significant redox peaks can be observed, with the oxidation peak and reduction peak located at 3.94V and 3.54V respectively. The voltage difference between the redox peaks is only 0.4V, indicating good redox reversibility. HE-LNM exhibits low electronic impedance before and after cycling. As shown in Figure S3, the electron transfer impedance before cycling is 108.3Ω, and the electron transfer impedance after cycling is 70.8Ω. The decrease in impedance after cycling is mainly due to the formation of stable interface SEI, which is beneficial to electron transport.

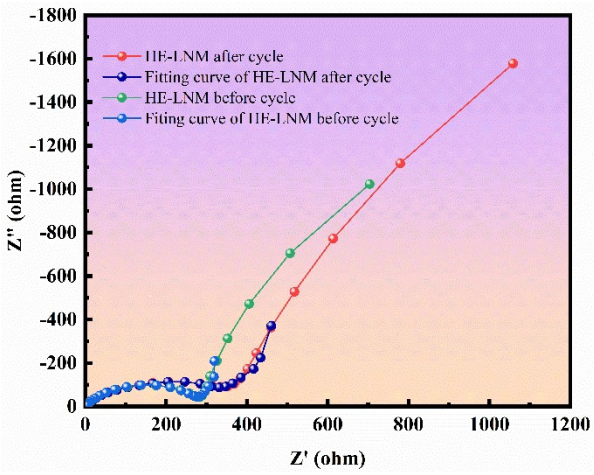

Figure S3 EIS.

Table S2. Comparison of this study with related studies.

Cathode material	Current density	Cycle number	Capacity retention	Journal and Ref.

HE-LNM	0.3C	350	81.56%	This article
HE-LNM	1C	100	85.75%	This article
$LiNiO_2$	0.3C	130	68%	Adv. Funct. Mater./ [4]
$LiNi_xFe_yAl_zO_2$	0.3C	200	72%	Journal of Power Sources[5]
$LiNi_{0.9}Mn_{0.1}O_2$	1C	180	65.6%	Journal of Alloys and Compounds/[6]
$LiNi_{0.5}Mn_{1.5}O_4$	0.3 C	300	67%	Energy & Environmental Science/[7]
$LiNi_{0.99}Mg_{0.01}O_2$	0.3C	130	76%	Adv. Funct. Mater./[4]
$LiNiO_2$	1C	200	55.2%	Journal of Alloys and Compounds/[8]
$LiNi_{0.8}Mn_{0.17}Fe_{0.03}O_2$	1C	100	80%	Braz. J. Chem. Eng./[9]

we have compared the material characterization results with other cathode materials under the same conditions as follows. Compared to other studies, HE-LNM demonstrated smaller harmful changes in the C-axis direction and a stable structure.

Table S3. The comparison of material characterization

Cathode material	Morphology	Change rate in the c-axis direction	R_{ct} after cycle	Phase transformation or the formation of cracks	Journal and Ref.
HE-LNM	spherical	1.39%	70.8	no	This article
$LiNiO_2$	spherical	unknown	unknown	Yes	ACS Energy Letters/[10]
LNMO	irregular	unknown	137.8	Yes	Nano letters/[11]
Fe-LNMO	irregular	unknown	113	Yes	Nano letters/[11]
Cl-LNMO	irregular	unknown	187	Yes	Nano letters/[11]
$LiNi_{0.9}Co_{0.1}O_2$	spherical	2.1%	90	Yes	Advanced Energy Materials/[12]
$LiNi_{0.9}Co_{0.05}Mn_{0.05}O_2$	spherical	1.7%	unknown	Yes	ACS Energy Letters/[13]

PC-NM91	irregular	unknown	658.7	Yes	ACS Sustainable Chemistry & Engineering/[14]
$LiNi_{0.9}Co_{0.05}Mn_{0.05}O_2$	spherical	5.7%	unknown	Yes	JACS/[15]
$LiNi_{0.7}Co_{0.15}Mn_{0.15}O_2$	spherical	5.0%	unknown	Yes	JACS/[15]
$LiNi_{0.7}Co_{0.15}Mn_{0.15}O_2$	spherical	4.5%	unknown	Yes	JACS/[15]
$LiNi_{1/3}Co_{1/3}Mn_{1/3}O_2$	spherical	5.1%	unknown	Yes	JACS/[15]

Refences

[1] Kresse, G. & Joubert, D., *Physical Review B*, **1999**, 59, 1758-1775.

[2] Perdew, J. P., Burke, K. & Ernzerhof, M., *Physical Review Letters*, **1996**, 77, 3865-3868.

[3] Grimme, S., Antony, J., Ehrlich, S. & Krieg, H., *The Journal of Chemical Physics*, **2010**, 132.

[4] Yi, M., Dolocan, A. & Manthiram, A., *Advanced Functional Materials*, **2023**, 33, 2213164.

[5] Muralidharan, N., Essehli, R., Hermann, R. P., Parejiya, A., Amin, R., Bai, Y., Du, Z. & Belharouak, I., *Journal of Power Sources*, **2020**, 471, 228389.

[6] Feng, H., Leng, Y., Chen, T., Sun, Y., Hai, C. & Zhou, Y., *Journal of Alloys and Compounds*, **2023**, 960, 170676.

[7] Yao, W., Chouchane, M., Li, W., Bai, S., Liu, Z., Li, L., Chen, A. X., Sayahpour, B., Shimizu, R., Raghavendran, G., Schroeder, M. A., Chen, Y.-T., Tan, D. H. S., Sreenarayanan, B., Waters, C. K., Sichler, A., Gould, B., Kountz, D. J., Lipomi, D. J., Zhang, M. & Meng, Y. S., *Energy & Environmental Science*, **2023**, 16, 1620-1630.

[8] Zhang, S., Gao, P., Wang, Y., Li, J. & Zhu, Y., *Journal of Alloys and Compounds*, **2021**, 885, 161005.

[9] Su, Y., Zhu, B., Zhang, Y., Meng, Q. & Dong, P., *Brazilian Journal of Chemical Engineering*, **2024**.

[10] Yoon, C. S., Jun, D.-W., Myung, S.-T. & Sun, Y.-K., *ACS Energy Letters*, **2017**, 2, 1150-1155.

[11] Nie, L., Wang, Z., Zhao, X., Chen, S., He, Y., Zhao, H., Gao, T., Zhang, Y., Dong, L., Kim, F., Yu, Y. & Liu, W., *Nano Letters*, **2021**, 21, 8370-8377.

[12] Aishova, A., Park, G.-T., Yoon, C. S. & Sun, Y.-K., *Advanced Energy Materials*, **2020**, 10, 1903179.

[13] Voronina, N., Sun, Y.-K. & Myung, S.-T., *ACS Energy Letters*, **2020**, 5, 1814-1824.

[14] Dai, P., Kong, X., Yang, H., Li, J., Zeng, J. & Zhao, J., *ACS Sustainable Chemistry & Engineering*, **2022**, 10, 4381-4390.

[15] Li, W., Asl, H. Y., Xie, Q. & Manthiram, A., *Journal of the American Chemical Society*, **2019**, 141, 5097-5101.